THE JOURNAL OF PHYSICAL CHEMISTRY C
A JOURNAL OF THE AMERICAN CHEMICAL SOCIETY

pubs.acs.org/JPCC

Article

Charge Transport in High-Entropy Oxides

Wojciech Skubida,* Daniel Jaworski, Aleksandra Mielewczyk-Gryń, Sebastian Wachowski, Tadeusz Miruszewski, Kacper Cichy, Konrad Świerczek, and Maria Gazda

Cite This: *J. Phys. Chem. C* 2023, 127, 14534−14544

Read Online

ACCESS | Metrics & More | Article Recommendations | Supporting Information

ABSTRACT: This work presents the results of research on the transport properties of the high-entropy $BaZr_{1/8}Hf_{1/8}Sn_{1/8}Ti_{1/8}Y_{1/8}In_{1/8}Sm_{1/8}Yb_{1/8}O_{3-x}$ perovskite oxide with special focus on proton transport. The presented study is part of broader work in which we focus on multiple different chemical compositions with the cation number varying from 5 up to 12 (in B-sublattice). The presence of proton defects is analyzed with thermogravimetry, whereas the results of electrochemical impedance spectroscopy in dry, H_2O-, and D_2O-containing synthetic air in the 300−800 °C temperature range enable the evaluation of the proton and deuterium conductivities. The isotope effect is observed and discussed. The obtained data allow us to establish the contribution of proton conductivity to the total one and the transport numbers for proton/deuterium conductivity. Based on the bulk and grain boundary conductivities, the potential at a grain boundary φ_0, Debye length L_D, and space-charge layer (SCL) thickness λ for proton defects is calculated. The potential barrier heights were found to be significantly lower than those observed for typical polycrystalline-doped barium zirconates. For the first time in the case of high-entropy oxides, the electrical conductivity relaxation (ECR) studies are performed, allowing the calculation of water kinetic coefficients. The ECR in the 300−600 °C temperature range revealed a single-fold nature, which indicates a negligible component of the electronic hole conductivity in the hydrated material. The chemical diffusion coefficient of water $D_{OH^\bullet}$ and the chemical surface exchange coefficient of water $k_{OH^\bullet}$ along with their activation energies are determined. The chemical diffusion coefficient $D_{OH^\bullet}$ is in a range of $10(1)^{-8}$−$10(1)^{-6}$ cm^2 s^{-1}, and the chemical surface exchange coefficient $k_{OH^\bullet}$ is in a range of $10(1)^{-6}$−$10(1)^{-4}$ cm s^{-1}.

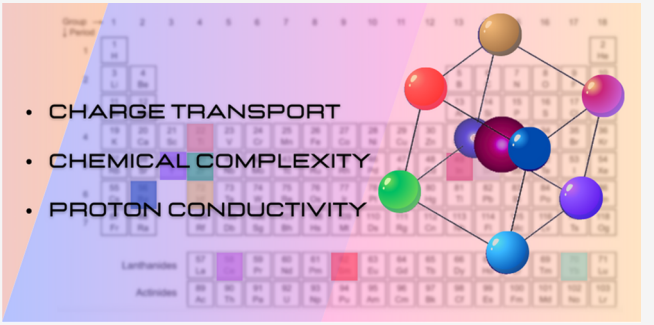

1. INTRODUCTION

Oxides are compounds in which both electronic- and ionic-type species could transport electric charge. In several oxides, for example, in perovskites based on barium zirconate or cerate in humidified atmospheres, the conduction of three types of charge carriers, i.e., oxygen ions, protons, and electron/holes, is possible. Charge transport processes may take place via a variety of conduction mechanisms: electrons/holes either hop between localized states or move over extended states in the conduction band, whereas ion transport occurs through defects, that is, vacancies, interstitial positions, dislocations, or grain boundaries. The presence of defects, especially point defects, may influence the concentration and mobility of both electronic and ionic charge carriers. What makes oxides even more interesting is cross effects, i.e., an influence of particular charge carrier fluxes one on another may occur. For example, Yoo et al.[1] observed the cross effect between the electronic and ionic fluxes in $Co_{1-x}O$. What is more, in the case of many oxides conducting protons and oxide ions, both types of charge carriers utilize the same defects, oxygen vacancies, so that they compete with one another.

The ABO_3 perovskite compounds, in which A and B are cations of different valence states and ionic radii, whereas the oxygen sublattice may show significant deviation from stoichiometry,[2] are especially disposed to be modified by using various substitutions. Therefore, perovskites are interesting candidates for tailoring their electrical properties by using multiple constituents. For instance, Jiang et al. demonstrated that aliovalent substitutions are possible in perovskites based on $Ba(Zr_{0.2}Sn_{0.2}Ti_{0.2}Hf_{0.2}Ce_{0.2})O_3$.[3] Donor- or acceptor-type substitutions are the most often used methods of tailoring the electrical conductivity of oxides. Recently, Yinchun Shi et al. reported the electrical properties of the $LaMnO_3$-based high-entropy perovskites.[4] They found that the electronic transport in high-entropy manganites in which the A-sublattice was occupied with five different cations occurs as small polaron hopping, whereas the value of conductivity depends on both the content of acceptor-type constituents, the cation size difference, and structural symmetry. Oxygen ion conductivity

Received: June 9, 2023
Revised: June 28, 2023
Published: July 12, 2023

was studied in fluorite-type oxides and was first reported by Gild et al. to be rather low, i.e., about 6×10^{-4} S cm^{-1} at 700 °C.[5] Further studies by Bonnett et al. showed higher values of conductivity in $Hf_{0.2}Zr_{0.2}Ce_{0.2}Y_{0.2}Gd_{0.2}O_{1.8}$ (2.5×10^{-3} S cm^{-1} at 700 °C),[6] which means that the tailoring of ionic conductivity in these materials is possible. The most spectacular ionic conductivity of high-entropy oxides was first reported in $(MgCoNiCuZn)_{0.67}Li_{0.33}O$ by Bérardan et al. who found a room-temperature Li-ion conductivity of 1 mS cm^{-1}.[7] Moreover, bulk room-temperature ionic conductivity exceeding 1 mS cm^{-1} in high-entropy NASICON compounds was studied by Zeng et al.[8] The authors suggested that the increased solubility of different cations in high-entropy oxides in comparison to those of the low-entropy ones leads to percolating transport networks thanks to the distribution in site energies. So far, only one report regarding proton conductivity in high-entropy oxides has been published.[9] The achieved values of conductivity were not high, but we believe the strategy of using high entropy as a way to both increase the solubility of acceptor constituents and enhance percolating networks that may also be applied to the group of proton-conducting oxides.

In this work, we present the properties of $BaZr_{1/8}Hf_{1/8}Sn_{1/8}Ti_{1/8}Y_{1/8}In_{1/8}Sm_{1/8}Yb_{1/8}O_{2.75}$, which is an exemplary member of multicomponent perovskites showing mixed conductivity. As a multicomponent oxide with the configurational entropy (calculated based on 10) equal to 1.76 R, which is larger than 1.5 R, it is a high-entropy oxide, though it is not an entropy-stabilized material. What is more, $BaZr_{1/8}Hf_{1/8}Sn_{1/8}Ti_{1/8}Y_{1/8}In_{1/8}Sm_{1/8}Yb_{1/8}O_{3-x}$ may be considered a very special composition in the family of multicomponent perovskites, since assuming an ideal random cation distribution, one may imagine the unit cell as consisting of Ba in the center and eight different B-cations in each corner of the cell. Special attention was focused on the properties related to proton transport. What is important, for the first time in high-entropy oxides, the chemical surface exchange coefficient $k_{OH^\bullet}$ and the chemical diffusion coefficient $D_{OH^\bullet}$ for the coupled ionic transport of water were determined.

2. METHODOLOGY

$BaZr_{1/8}Hf_{1/8}Sn_{1/8}Ti_{1/8}Y_{1/8}In_{1/8}Sm_{1/8}Yb_{1/8}O_{3-x}$ was synthesized by a high-temperature solid-state route. Respective oxides (ZrO_2, HfO_2, SnO_2, TiO_2, Y_2O_3, In_2O_3, Sm_2O_3, Yb_2O_3, Alfa Aesar 99.9% purity) and barium carbonate (abcr GmbH, 98% purity) in stoichiometric proportions were ball-milled with isopropanol. The mixed reagents were then dried at 80 °C and calcined at 950 °C in a flow of synthetic air for 24 h. The calcined powder was mixed with 1 wt % of PVB (poly(vinyl butyral-*co*-vinyl alcohol-*co*-vinyl acetate)) and isopropanol and dried for 24 h at 80 °C. The powders were mixed with 1 wt % of NiO, sieved through a 100 μm mesh, and uniaxially pressed into pellets. PVB serves as an additive, increasing the green body density of the material, while the addition of NiO improves sinterability. The amount of nickel oxide introduced into the system is only about 1 wt %, which corresponds to approximately 4 molar %. If a fraction of nickel enters the lattice position of the B-cations, it would result in a very low concentration of additional acceptors compared to the amount derived from the acceptor substituents in the B-sublattice. Therefore, this effect did not affect the properties of the studied material. The pellets were sintered at 1530 °C in the air for 10 h with a 5 °C min^{-1} heating/cooling rate.

The crystal structure was investigated by X-ray diffraction (XRD) at room and elevated temperatures (HT-XRD). Measurements were conducted using Cu Kα radiation on a Panalytical Empyrean diffractometer equipped with a PIXcel3D detector. For high-temperature measurements, carried out in a synthetic airflow (H_2O content <3 ppm), an Anton Paar HTK 1200N oven chamber was mounted. Structural data were analyzed using GSAS II software based on the Rietveld method. For the basis of the model, a modified crystallography information file (*.cif*) for $BaZrO_3$ ($Pm\bar{3}m$ space group) was utilized.[11]

The microstructure and elemental composition of the samples were investigated by an FEI Quanta FEG 250 scanning electron microscope (SEM) with an EDAX Apollo energy-dispersive spectrometer (EDS). The micrographs were obtained simultaneously using secondary electrons (SEs) and back-scattered electrons (BSEs) with Everhart−Thornley detector (ETD) and a low-voltage high-contrast detector (vCD), respectively. The measurements were carried out in a high-vacuum mode with an acceleration voltage of 20 kV for the microstructural analysis, while for EDS scans, 30 kV was used.

To investigate water incorporation into the sample, two thermogravimetric (TG) experiments were performed. In the first approach, a powdered sample was annealed at 300 °C for 24 h in a humidified (p_{H_2O} ca. 2.3×10^{-2} atm.) synthetic airflow. Next, the mass of the powdered sample was measured in a synthetic airflow on a TA Q5000 IR thermobalance up to 850 °C with a 5 °C min^{-1} heating/cooling rate. Measurements were accompanied by the analysis of the released gas by mass spectrometry (Pfeiffer Vacuum ThermoStar). The second type of experiment was performed on a Netzsch STA 449 to measure the water uptake. It was performed in either air or nitrogen atmosphere. A powdered sample was annealed at 800 °C for 5 h in dry gas (p_{H_2O} ca. 5.0×10^{-5} atm.) to remove water and surface carbon dioxide. Then, it was cooled to 300 °C and kept at this temperature for 2 h. After that, the purge gas (dry synthetic air/nitrogen, 20 mL min^{-1}) was switched to the humidified air/nitrogen (p_{H_2O} ca. 2.3×10^{-2} atm.), the sample remained in this atmosphere for 2 h and then the gas was switched back to the dry one for another 2 h. The time evolution of weight changes related to the water sorption and desorption was recorded during both stages of the analysis. The difference between the mass recorded in the dry and wet atmospheres (Δm_{H_2O}) allowed us to estimate the molar protonic defect concentration [$OH_O^\bullet$]. Before the TG experiments, the blank correction run was performed. In all experiments, nitrogen was used as the protective gas (20 mL min^{-1}) for the thermobalance mechanism.

Electrical properties of the $BaZr_{1/8}Hf_{1/8}Sn_{1/8}Ti_{1/8}Y_{1/8}In_{1/8}Sm_{1/8}Yb_{1/8}O_{3-x}$ oxide were studied by electrical impedance spectroscopy (EIS) using a Gamry 3000 potentiostat. The relative density of the pellets was over 95%, and they were 11 mm in diameter and 0.8 mm thick. Before the measurements, the pellets were polished and Pt paste (Electro-Science Laboratories, Inc.) along with thin Pt wires was applied. Next, the samples were heat-treated at 930 °C for 2 h with a 3 °C min^{-1} heating/cooling rate. The samples were mounted on a Probostat holder and inserted into a tube furnace. The measurements were carried out in the 300−800 °C temperature range in dry, H_2O-, and D_2O-containing synthetic air (p_{H_2O} ca. 10^{-5} atm., p_{H_2O} ca. 10^{-2} atm.

https://doi.org/10.1021/acs.jpcc.3c03906
J. Phys. Chem. C 2023, 127, 14534−14544

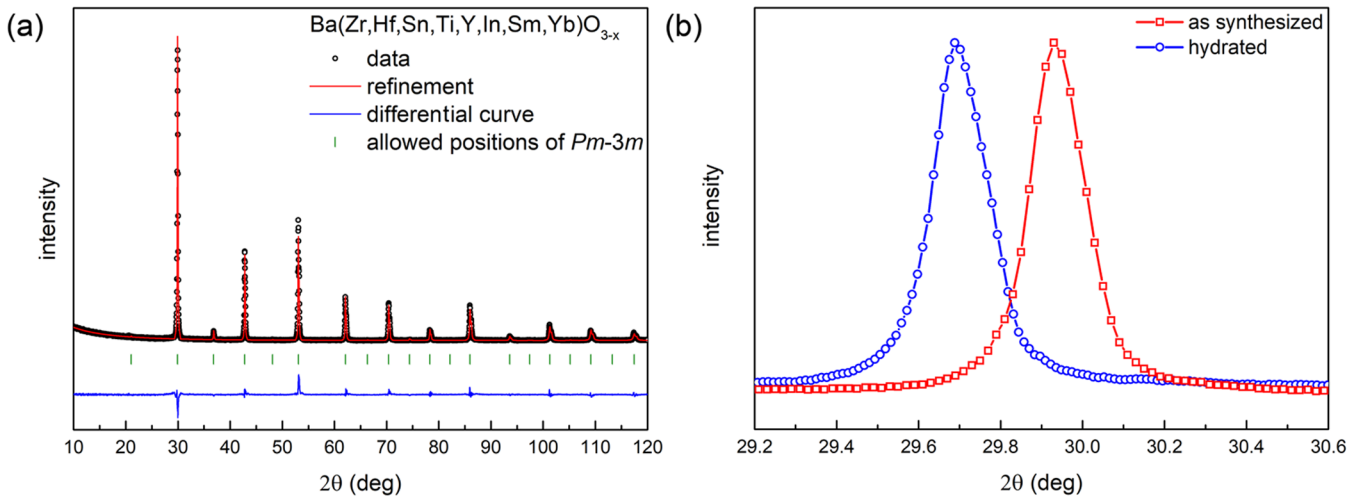

Figure 1. (a) Diffractogram with the Rietveld profile for as-synthesized $BaZr_{1/8}Hf_{1/8}Sn_{1/8}Ti_{1/8}Y_{1/8}In_{1/8}Sm_{1/8}Yb_{1/8}O_{3-x}$. Data collected at RT; (b) the (110) reflection for the as-synthesized and hydrated samples at RT.

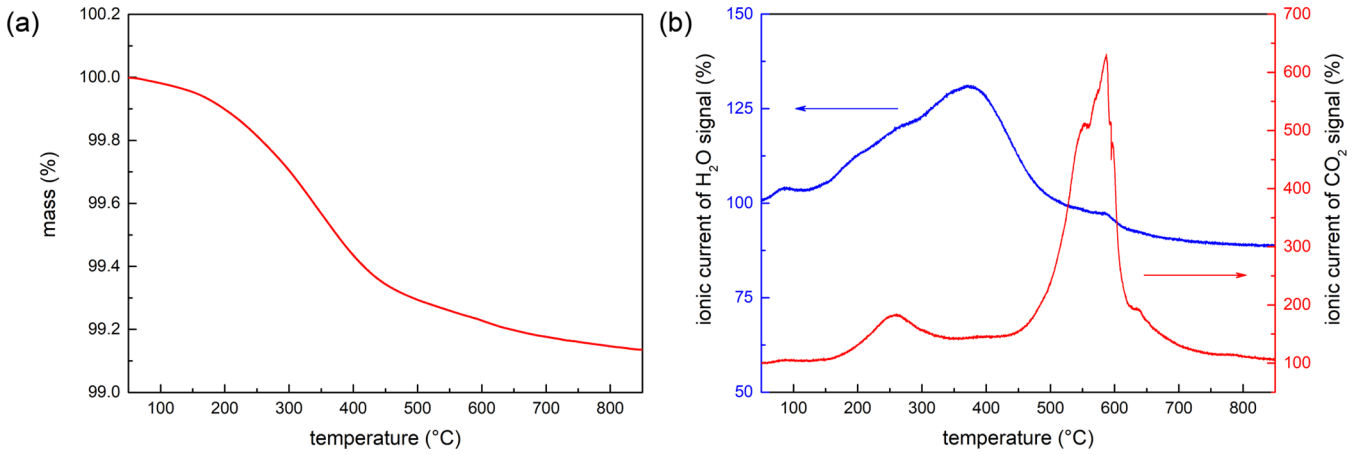

Figure 2. (a) TG curves recorded during heating in synthetic air for the previously hydrated $BaZr_{1/8}Hf_{1/8}Sn_{1/8}Ti_{1/8}Y_{1/8}In_{1/8}Sm_{1/8}Yb_{1/8}O_{3-x}$ sample with gas analysis data of (b) H_2O- and CO_2-related relative signals.

and p_{D_2O} ca. 10^{-2} atm., respectively) in 1 Hz to 1 MHz frequency range. All of the measurements were conducted in synthetic air (<5 ppm H_2O) with a drying stage containing silica gel and P_2O_5 and humidifying stage containing the supersaturated solution of KBr. Additionally, the entire gas system is made of copper pipes, ensuring a significant reduction in the permeability of water from the atmospheric air to the system. Gathered data were analyzed with Scribner Associates Inc. ZView software. Approximated values of partial conductivity were calculated as the difference between the conductivities in wet (H_2O- and D_2O-containing) and dry conditions (i.e., $\sigma_{H/D} = \sigma_{wet(H/D)} - \sigma_{dry}$). Transport numbers have been estimated as the ratio of the partial proton/deuterium conductivity and the total conductivity in humidified conditions (i.e., $t_{H/D} = \sigma_{H/D}/\sigma_{wet(H/D)}$).

To find the diffusion coefficient, D, and surface exchange coefficient, k, conductivity relaxation experiments were performed in the 300−600 °C temperature range. Isothermal EIS measurements after an abrupt atmosphere change (from dry to wet conditions) allowed us to determine the change in conductivity as a function of time. Such data were normalized and refined utilizing ECRTOOLS (Matlab toolbox for fitting and interpreting ECR data), which enabled us to calculate $D_{OH^\bullet}$ and, in some cases, $k_{OH^\bullet}$ coefficients.[12] The obtained values were plotted in Arrhenius-type coordinates, and activation energies of respective processes were calculated.

3. RESULTS AND DISCUSSION

3.1. Crystal Structure and Microstructure. Figure 1a presents an X-ray diffractogram with a Rietveld profile for the as-synthesized $BaZr_{1/8}Hf_{1/8}Sn_{1/8}Ti_{1/8}Y_{1/8}In_{1/8}Sm_{1/8}Yb_{1/8}O_{3-x}$ oxide. The pattern corresponds to the cubic crystal structure (space group $Pm\bar{3}m$), which is consistent with the predictions based on the tolerance factor t = 0.98 (where $t = \frac{r_A + r_O}{\sqrt{2}(r_B + r_O)}$ and r_A, r_B, and r_O are ionic radii of the A-constituent, B-constituent, and oxygen, respectively).[13] Since the proton conduction of an oxide requires humidified environment, it is important to check whether the water exposure affects the material phase composition and structure. As shown in Figure S1, the $BaZr_{1/8}Hf_{1/8}Sn_{1/8}Ti_{1/8}Y_{1/8}In_{1/8}Sm_{1/8}Yb_{1/8}O_{3-x}$ oxide after annealing at 300 °C for 24 h in the humidified (p_{H_2O} ca. 2 × 10^{-2} atm.) synthetic airflow remained single-phase cubic perovskite. The Rietveld analysis results showed that the presence of proton defects causes an increase in the unit cell volume. It is illustrated in Figure 1b, presenting a shift of the

https://doi.org/10.1021/acs.jpcc.3c03906
J. Phys. Chem. C 2023, 127, 14534−14544

(110) reflection toward lower 2θ angles for the hydrated sample in comparison to that of the dried one. A chemical expansion caused by hydration is typical of perovskite proton conductors, in which the hydration is related to the formation of two proton defects accompanied by the disappearance of one oxygen vacancy (eq 1). The chemical strain, stemming from the relative change of the unit cell parameter of $BaZr_{1/8}Hf_{1/8}Sn_{1/8}Ti_{1/8}Y_{1/8}In_{1/8}Sm_{1/8}Yb_{1/8}O_{3-x}$ upon hydration, was 0.39%. This value is similar to that of $BaZr_{0.8}Y_{0.2}O_{3-x}$ (0. 34%) but lower than the chemical strain in $BaZr_{0.5}In_{0.5}O_{3-x}$ (1.07%) in which, similar to $BaZr_{1/8}Hf_{1/8}Sn_{1/8}Ti_{1/8}Y_{1/8}In_{1/8}Sm_{1/8}Yb_{1/8}O_{3-x}$, 50% of the B-constituents are acceptors.[14]

To study the material homogeneity, grain size, and density, SEM measurements with EDS analysis were performed. In Figure S2, SEM micrographs of a cross section of the $BaZr_{1/8}Hf_{1/8}Sn_{1/8}Ti_{1/8}Y_{1/8}In_{1/8}Sm_{1/8}Yb_{1/8}O_{3-x}$ sample obtained using secondary electrons (SEs) and back-scattered electrons (BSEs) are shown. As can be noticed, the sample was dense and the average grain size was found to be ~9 μm. The BSE image does not show visible precipitates, indicating a single-phase composition. The EDS analysis confirmed the uniform distribution of atoms in the entire volume of the sample (Figures S3 and S4 and Table S1).

3.2. Proton Defects. Proton defects in $BaZr_{1/8}Hf_{1/8}Sn_{1/8}Ti_{1/8}Y_{1/8}In_{1/8}Sm_{1/8}Yb_{1/8}O_{3-x}$ were studied with thermogravimetric analysis and high-temperature XRD. Figure 2 shows TG curves and gas analysis data recorded in synthetic air for the sample that was previously hydrated at 300 °C for 24 h. Figure 3 presents mass changes during isothermal

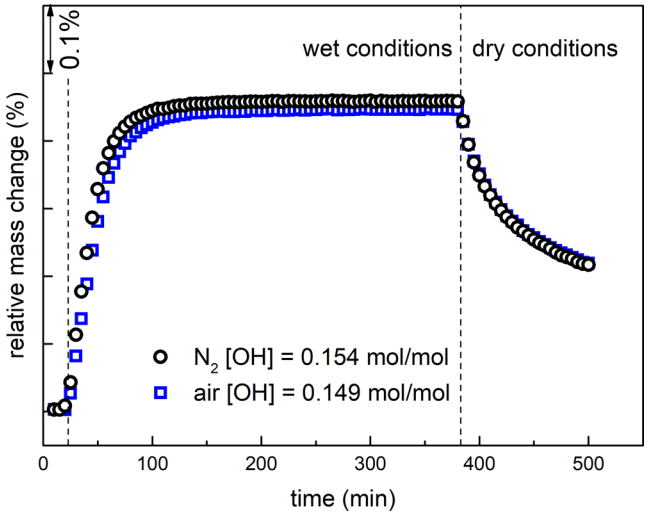

Figure 3. Mass change recorded after an isothermal switch at 300 °C between dry and humidified nitrogen (black circles) and air (blue squares).

switches from dry to humidified air and nitrogen at 300 °C, while the results of the HT-XRD measurements are presented in Figure 4. As shown in Figure 2a, during heating, 0.6% of relative mass loss can be observed below 500 °C. This may be attributed mainly to water release and partially to CO_2 desorption (Figure 2b) from the surface. It has to be emphasized that the H_2O and CO_2 signals are not quantitative but qualitative. The CO_2 peak at 580 °C can be related to the further release of surface-bonded complex carbon compounds, e.g., oxyhydroxycarbonates.[15,16]

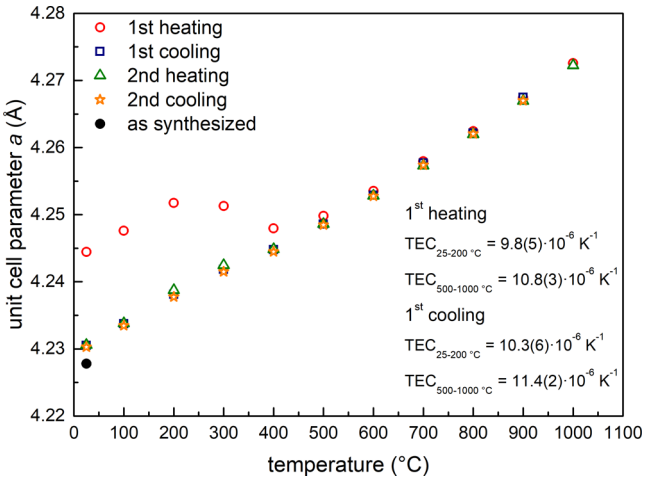

Figure 4. Temperature dependence of unit cell parameter for hydrated $BaZr_{1/8}Hf_{1/8}Sn_{1/8}Ti_{1/8}Y_{1/8}In_{1/8}Sm_{1/8}Yb_{1/8}O_{3-x}$, recorded during heating and cooling in dry synthetic air. As the estimated error values are very low (see Table S2), thus the error bars are not included as they would be smaller than the data points in the plots.

The time evolution of mass, for the sample previously dried at 800 °C for 5 h, after the switches from dry to humidified air and nitrogen at 300 °C shown in Figure 3 was analyzed to evaluate the proton defect content. In both cases, the process takes place in one step and the relative mass change observed after the switch is about 0.46% (0.154 mol mol^{-1}) and 0.44% (0.149 mol mol^{-1}) in nitrogen and synthetic air atmospheres, respectively. The difference between the relative mass changes recorded in nitrogen and air atmospheres is caused by different contents of oxygen vacancies formed during the annealing at 800 °C. Nevertheless, the difference is small, which suggests that in both atmospheres, water incorporation occurs through the hydration process described by eq 1

$$H_2O + O_O^X + V_O^{\bullet\bullet} = 2OH_O^{\bullet} \quad (1)$$

where $V_O^{\bullet\bullet}$, O_O^X, and $OH_O^{\bullet}$ denote the Kröger–Vink symbols of oxygen vacancy, lattice oxygen, and proton defect, respectively.

The content of proton defects observed in hydrated $BaZr_{1/8}Hf_{1/8}Sn_{1/8}Ti_{1/8}Y_{1/8}In_{1/8}Sm_{1/8}Yb_{1/8}O_{3-x}$ is more than twice higher compared to those in yttrium-doped barium zirconate in similar conditions ($BaZr_{0.7}Y_{0.3}O_{3-x}$ – 0.072 mol mol^{-1} in the air)[17] and more than nine times higher than previously reported by us for high-entropy oxides (e.g., 0.016 mol mol^{-1} in $BaZr_{0.2}Sn_{0.2}Ti_{0.2}Hf_{0.2}Y_{0.2}O_{3-x}$ in the air).[9] Norby et al.[18] suggested a relationship (eq 2) between the enthalpy of hydration ΔH and the difference in the Allred–Rochow electronegativity ΔX_{B-A} of B- and A-site cations in ABO_3 perovskites

$$\Delta H = 400\Delta X_{B-A} - 180 \text{ [kJ mol}^{-1}\text{]} \quad (2)$$

Taking the Allred–Rochow electronegativities of 0.97, 1.22, 1.23, 1.72, 1.44, 1.11, 1.49, 1.07, and 1.06 for Ba, Zr, Hf, Sn, Ti, Y, In, Sm, and Yb, respectively,[19] the difference ($\chi_B - \chi_A$) of $BaZr_{1/8}Hf_{1/8}Sn_{1/8}Ti_{1/8}Y_{1/8}In_{1/8}Sm_{1/8}Yb_{1/8}O_{3-x}$ is 0.3225, and the enthalpy of hydration for that oxide can be estimated as −51 kJ mol^{-1}. This means a more exothermic hydration process in comparison to the previous high-entropy oxides (e.g., $BaZr_{0.2}Sn_{0.2}Ti_{0.2}Hf_{0.2}Y_{0.2}O_{3-x}$—$\Delta H$ = −40 kJ mol^{-1}) reported by us.[9] This is also in the vicinity of the ΔH obtained by thermogravimetric studies for yttrium-doped barium

https://doi.org/10.1021/acs.jpcc.3c03906
J. Phys. Chem. C 2023, 127, 14534−14544

zirconate, which, depending on the dopant concentration, was between −18 and −141 kJ mol^{-1}.[17] The detailed study of the energetics of hydration, as well as the temperature-dependent proton concentration, of $BaZr_{1/8}Hf_{1/8}Sn_{1/8}Ti_{1/8}Y_{1/8}In_{1/8}Sm_{1/8}Yb_{1/8}O_{3-x}$ and other high-entropy perovskites is a matter of our separate work.[20]

Figure 3 also shows that after the switch from the humidified to dry conditions, the mass does not go back to the initial value as quickly as in the opposite case. This may indicate that a certain number of protons remains in the structure of the compound. Such behavior may indicate slow kinetics of dehydration of the material.

As mentioned in Section 3.1, the presence of proton defects influences the structural properties of the oxide by the chemical expansion caused by hydration, which was observed by XRD. The Rietveld analysis of the high-temperature XRD results of the previously hydrated oxide allowed us to determine the temperature evolution of the unit cell parameter (Figure 4 and Table S2). As shown by TGA, heating the oxide containing proton defects in dry synthetic air (p_{H_2O} ca. 10^{-5} atm.) causes water release from the material. This explains why during the first heating in the 200−400 °C temperature range, the unit cell parameter changes nonmonotonically. Similar behavior has been found for other perovskite-type oxides, e.g., barium titanates,[21] zirconates,[22] or indates,[23] while for high-entropy material, it was observed for the first time. During further cooling−heating cycles, still, a small nonlinearity can be seen below 500 °C. Moreover, a slightly lower unit cell parameter of the as-synthesized material than that of the sample after a few heating/cooling cycles in dry air suggests that during the heat treatment, the sample did not release all of the incorporated water. These findings support the idea of slow dehydration kinetics first indicated by the results of TG analysis.

Two different values of thermal expansion coefficients (TECs) were found below 200 °C and above 500 °C. In the case of the first heating of the hydrated $BaZr_{1/8}Hf_{1/8}Sn_{1/8}Ti_{1/8}Y_{1/8}In_{1/8}Sm_{1/8}Yb_{1/8}O_{3-x}$, TEC values were 9.8(5) × 10^{-6} K^{-1} and 10.8(3) × 10^{-6} K^{-1} in lower- (25−200 °C) and higher (500−1000 °C)-temperature ranges, respectively. The obtained TEC values are comparable to the other perovskite proton conductors,[24] suggesting that the high-entropy configuration of this material does not affect significantly the average bond anharmonicity.

3.3. Transport Properties. The Nyquist impedance spectra as well as the details of the analysis of the impedance results are presented in the SI (Figure S5). Based on the impedance data gathered in different conditions, the total, bulk, and specific grain boundary conductivities of $BaZr_{1/8}Hf_{1/8}Sn_{1/8}Ti_{1/8}Y_{1/8}In_{1/8}Sm_{1/8}Yb_{1/8}O_{3-x}$ were determined. The results are shown in Figure 5. The total conductivity in various conditions (Figure 5a and Table S3) is between 10^{-7} and 10^{-3} S cm^{-1} in the temperature range of 300−800 °C. In the studied temperature range, in H_2O- and D_2O-containing air, the values of total conductivity are higher compared to those of the dry conditions; however, the difference decreases with increasing temperature. This is typical of oxides in which proton defects contribute to the total conductivity. At about 500 °C, the slopes of the $\sigma(T)$ plots in all atmospheres change, which suggests a change in the conduction mechanism. Additionally, the proton mobility was calculated. At 700 °C, the mobility is 3.5 × 10^{-6} cm^2 V^{-1} s^{-1},

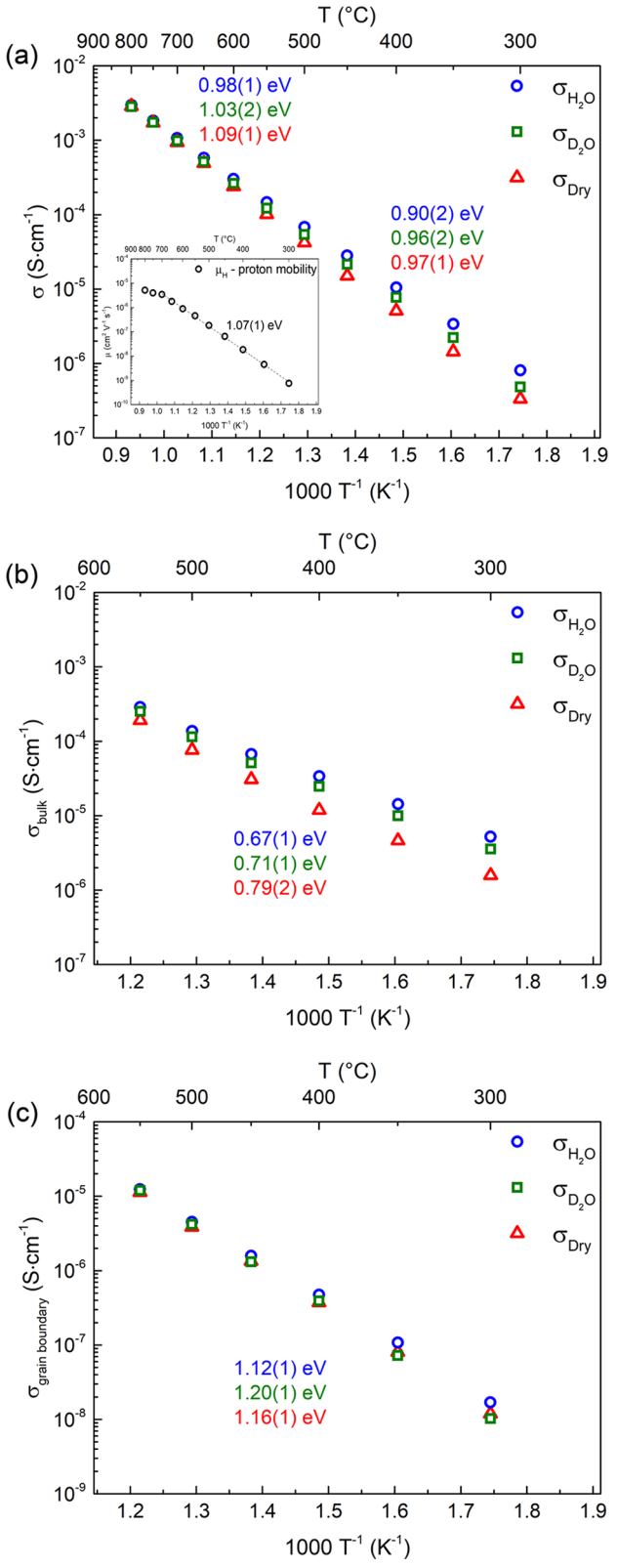

Figure 5. Temperature dependence, shown in Arrhenius-type coordinates, of the (a) total electrical conductivity; inset, calculated proton mobility (Figure S7); (b) bulk conductivity; and (c) specific grain boundary conductivity of the $BaZr_{1/8}Hf_{1/8}Sn_{1/8}Ti_{1/8}Y_{1/8}In_{1/8}Sm_{1/8}Yb_{1/8}O_{3-x}$ sample in dry, H_2O- and D_2O-containing air. For additional information, see Figure S8. The estimated error is lower than 10%; thus, the error bars are not included as they would be smaller than the data points in the plots.

https://doi.org/10.1021/acs.jpcc.3c03906
J. Phys. Chem. C 2023, 127, 14534−14544

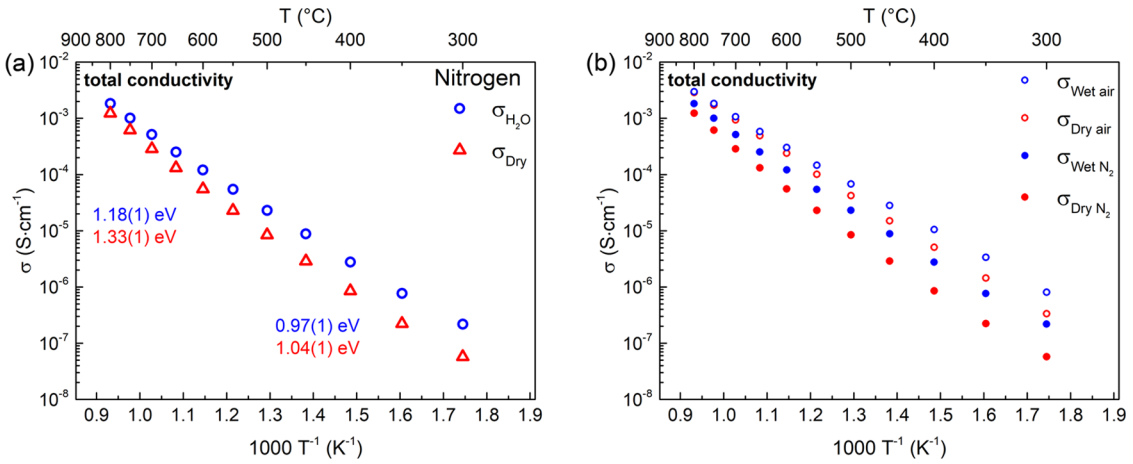

Figure 6. Temperature dependence, shown in Arrhenius-type coordinates, of the (a) total electrical conductivity in dry and H_2O-wet nitrogen, along with the activation energies, and (b) comparison of the total conductivity in dry and H_2O-wet either synthetic air or nitrogen. The estimated error is lower than 10%; thus, the error bars are not included as they would be smaller than the data points in the plots.

which is about one order of magnitude lower than for $BaCe_{0.65}Zr_{0.2}Y_{0.15}O_{3-\delta}$ for which the mobility of protons is 7.26×10^{-5} cm^2 V^{-1} s^{-1}.[25] Such a difference may be caused by the structural distortions that appear in such a multicomponent perovskite oxide decreasing the mobility of protons. In Figure 5b,c, the separated bulk and specific grain boundary conductivities in different atmospheres are shown. As can be noticed, the specific grain boundary conductivity is approximately 2 orders of magnitude lower than that of the bulk conductivity. Such behavior is typical of the $BaZrO_3$ system as in most cases the grain boundaries have a blocking character for ionic conduction.[26,27]

Additionally, the conductivity measurements were conducted in dry and wet nitrogens. The results are presented in Figure 6. First of all, the conductivity is lower in N_2 with respect to air regardless of the humidity. However, the difference between dry and wet conditions is larger than in air. Such behavior is expected as the pO_2 is decreased, since the concentration of electron−holes decreases and oxygen vacancies increase. The electron−hole mobility is much higher than the vacancies; thus, the reduction in their concentration leads to a decrease of the total conductivity. Due to the more ionic nature of conductivity in N_2, the activation energies are slightly higher than those calculated in the synthetic air. On the other hand, both reduced contribution of holes and increase of oxygen vacancy concentration lead to higher hydration level and larger difference between conductivity in dry and wet conditions, which are observed.

To analyze the contribution of proton conductivity to the total one, the conductivity isotope effect was studied (in synthetic air) and the transport numbers for proton/deuterium conductivity were evaluated. In Figure 7, the ratios of bulk conductivity in H_2O- and D_2O-containing air as a function of inverted temperature are presented. The $\sigma_{bulk-H_2O}/\sigma_{bulk-D_2O}$ ratio is 1.5 at 300 °C, and with increasing temperature, it decreases to 1.2 at 500 °C, reflecting a decreasing proton/deuteron contribution to the bulk conductivity. As the difference between activation energies of conductivity in H_2O- and D_2O-humidified atmospheres is observed, the conductivity isotope effect can be explained by the semi-classical model.[28] The observed difference between activation energies of bulk conductivity (0.04 eV) is within the model

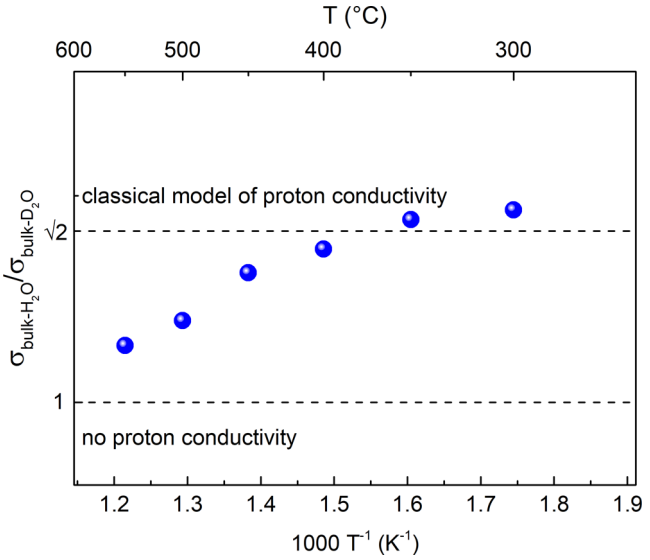

Figure 7. Ratios of bulk electrical conductivity in H_2O- and D_2O-containing synthetic air. Horizontal lines mark $\sigma_{bulk-H_2O}/\sigma_{bulk-D_2O}$ equal to $\sqrt{2}$ (classical model of ideal proton conductor)[28] and 1 (nonproton conductor).

limits $\Delta E_a \leq 0.055$ eV,[29] while that for grain boundary conductivity (0.08 eV) is higher. The observed isotopic effect shows that proton conduction occurs by the Grotthuss mechanism.[28]

The proton and deuterium conductivities and corresponding transport numbers were calculated utilizing eqs 3 and 4[30]

$$\sigma_{H/D} = \sigma_{wet(H/D)} - \sigma_{dry} \quad (3)$$

$$t_{H/D} = \sigma_{H/D}/\sigma_{wet(H/D)} \quad (4)$$

where $\sigma_{H/D}$ is the proton/deuterium conductivity, $\sigma_{wet(H/D)}$ is the total conductivity in the H_2O/D_2O-humidified atmosphere, σ_{dry} is the total conductivity in dry conditions, and $t_{H/D}$ is the proton/deuterium transport number. The results are collected in Table 1. The comparison of these values with those reported for other materials is not straightforward because of differences in experimental conditions used in different works. For example, Han et al. showed transport

https://doi.org/10.1021/acs.jpcc.3c03906
J. Phys. Chem. C 2023, 127, 14534−14544

Table 1. Partial Electrical Conductivity and Transport Numbers of the $BaZr_{1/8}Hf_{1/8}Sn_{1/8}Ti_{1/8}Y_{1/8}In_{1/8}Sm_{1/8}Yb_{1/8}O_{3-x}$ Perovskite

	proton/deuterium conductivity $\sigma_{H/D} = \sigma_{wet(H/D)} - \sigma_{dry}$ (S cm^{-1})			proton/deuterium transport number $t_{H/D} = \sigma_{H/D}/\sigma_{wet(H/D)}$		
			Total Electrical Conductivity			
T	800 °C	700 °C	600 °C	500 °C	400 °C	300 °C
σ_H	$1.18(1) \times 10^{-4}$	$1.29(1) \times 10^{-4}$	$6.21(1) \times 10^{-5}$	$2.61(1) \times 10^{-5}$	$5.40(1) \times 10^{-6}$	$4.72(1) \times 10^{-7}$
t_H	0.04(1)	0.12(1)	0.21(1)	0.38(1)	0.51(1)	0.59(1)
σ_D	-	$4.21(1) \times 10^{-5}$	$2.36(1) \times 10^{-5}$	$1.21(1) \times 10^{-5}$	$2.66(1) \times 10^{-6}$	$1.49(1) \times 10^{-7}$
t_D	-	0.04(1)	0.09(1)	0.22(1)	0.34(1)	0.31(1)
			Bulk Electrical Conductivity			
T	800 °C	700 °C	600 °C	500 °C	400 °C	300 °C
σ_H				$6.11(1) \times 10^{-5}$	$2.20(1) \times 10^{-5}$	$3.65(1) \times 10^{-6}$
t_H				0.44(1)	0.65(1)	0.70(1)
σ_D				$3.84(1) \times 10^{-5}$	$1.29(1) \times 10^{-5}$	$1.99(1) \times 10^{-6}$
t_D				0.33(1)	0.52(1)	0.56(1)

numbers of $BaZr_{0.9}Y_{0.1}O_{3-x}$ at 600 °C in a wet oxidizing atmosphere reported in different works between 0.07 and 0.6.[31] Nevertheless, the results show that the contribution of proton conduction in $BaZr_{1/8}Hf_{1/8}Sn_{1/8}Ti_{1/8}Y_{1/8}In_{1/8}Sm_{1/8}Yb_{1/8}O_{3-x}$ is significant at temperatures below 500 °C, while at higher temperatures, other charge carriers, i.e., oxygen vacancies and electron−holes, dominate. This agrees well with the TG and isotope effect results.

The activation energy of total conductivity in wet air below 500 °C (0.9 eV) compared to $BaZr_{0.9}Sc_{0.1}O_3$ (0.72 eV), $BaZr_{0.85}Sc_{0.05}Yb_{0.05}O_3$ (0.57 eV)[32] is higher, while it is comparable to that of $BaHf_{0.9-x}In_xSn_{0.1}O_{3-\delta}$ (0.94 eV for x = 0.1 and 0.15, 0.85 eV for x = 0.2)[33] and $BaZr_{0.8}M_{0.2}O_{3-x}$ for which the activation energy of conductivity in wet argon was found to be 0.83−1.0 eV for M = Sc, In, Lu, Y, and Sm.[34] On the other hand, Zhu and Wang reported the activation energy of the total conductivity of $BaZr_{0.8}Y_{0.2-x}Sm_xO_{3-\delta}$ (x = 0, 0.05, 0.1, 0.15, 0.2) in wet air as 0.96−0.97 eV.[35] Total conductivity and its activation energy are an important property, especially from the point of view of future practical applications. It depends on bulk and grain boundary conductivities.

The activation energy of bulk conductivity in humidified air below 500 °C (0.67 eV) is higher than that observed in acceptor-doped barium zirconate, which is usually between 0.4 and 0.6 eV.[34,36] Experimentally determined activation energy is composed of the contributions from energy barriers for the O−H bond rotation and proton hopping as well as of proton trapping energy. Recently, Draber et al. using the DFT and kinetic Monte Carlo methods discussed how the properties, content, and superstructures formed by different acceptors influence proton mobility in barium zirconate.[37,38] They found the barriers for the O−H rotation independent of the type of studied acceptors (Ga, Sc, In, Y, Gd), while the barriers for proton hopping are similar to one another for the most favorable hopping neighborhood, which is about 0.2−0.4 eV. On the other hand, in the case of high acceptor contents, the energetically unfavorable jumps in the neighborhood of two or three acceptor ions cannot be avoided. For instance, the energy barrier associated with the jumps in the vicinity of two and three yttrium ions was calculated as 0.52−0.58 and 0.66 eV, respectively.[38] This means that the contribution of such jumps may be one of the reasons for the relatively high activation energy of bulk conductivity in the here-studied high-entropy oxide. What regards proton trapping in multicomponent perovskites is that it has not been investigated so far; however, based on the relatively high activation energy of bulk conductivity in the $BaZr_{1/8}Hf_{1/8}Sn_{1/8}Ti_{1/8}Y_{1/8}In_{1/8}Sm_{1/8}Yb_{1/8}O_{3-x}$ oxide, proton trapping seems a possible reason. Trapping proton energy was analyzed in simpler systems; for example, Yamazaki et al., in $Ba_{0.97}Zr_{0.79}Y_{0.21}O_{3-x}$, determined it as approximately 0.3 eV.[39] A very interesting analysis of proton trapping was carried out by Draber et al. who found that the highest proton mobility in $BaZr_{1-x}Y_xO_3H_x$, is achieved for x = 0.25, especially if the acceptors form the body-centered cubic superstructure, whereas in the case of x = 0.5, a random distribution of acceptors is beneficial. In the case of high-entropy $BaZr_{1/8}Hf_{1/8}Sn_{1/8}Ti_{1/8}Y_{1/8}In_{1/8}Sm_{1/8}Yb_{1/8}O_{3-x}$, we assume that all constituents are randomly distributed. Nevertheless, each acceptor is expected to differ in trapping behavior and some of them, for instance, the largest samarium in the neighborhood of the smallest titanium, may form deep traps, which could effectively decrease the mobility of proton defects.[40]

The activation energy of conductivity related to the grain boundaries is higher than that of the bulk, meaning that charge carriers experience higher potential energy barriers. So far, it has been suggested that the main source of the potential barrier energy related to grain boundaries is the space charge, e.g., 41. A grain boundary in a polycrystalline oxide consists of a GB core with a maximum of positive potential energy and two adjacent space-charge layers (SCLs). The positive GB charge induces the depletion of the adjacent regions in the positively charged mobile defects, i.e., oxygen vacancies and proton defects. The mobile defects' depletion in the space-charge layers is considered the main reason for the grain boundary blocking effect.[42] The space-charge layer thickness is characterized by the Debye length. To calculate the barrier potential and space-charge layer thickness related to the grain boundaries, we used an approach proposed by Fleig et al.,[43] within which the potential φ_0 at a grain boundary can be calculated using the formula

$$\frac{\sigma_{bulk}}{\sigma_{GB-spec}} = \frac{e^{Ze\varphi_0/kT}}{2\frac{Ze\varphi_0}{kT}} \quad (5)$$

where σ_{bulk} is the conductivity of the grain bulk, $\sigma_{GB\text{-}spec}$ ($\sigma_{GB-spec} = \frac{\sigma_{GB}C_B}{C_{GB}}$; C_{GB} and C_B are the capacitance of the grain boundary and bulk, respectively) is the conductivity of a specific grain boundary, Z is the charge of the dominating

https://doi.org/10.1021/acs.jpcc.3c03906
J. Phys. Chem. C 2023, 127, 14534−14544

charge carrier in given conditions, and e is the elementary charge. Furthermore, since the proton concentration at 300 °C is known, the Debye length L_D and space-charge layer (SCL) thickness λ can be calculated using the equations

$$L_D = \sqrt{\frac{kT\varepsilon\varepsilon_0}{2e^2c}} \tag{6}$$

$$\lambda = 2L_D\sqrt{\frac{2e\varphi_0}{kT}} = \sqrt{\frac{2\varepsilon\varepsilon_0\varphi_0}{ec}} \tag{7}$$

where c is the acceptor concentration, ε is the relative dielectric constant, and e is the elemental charge. The relative dielectric constant was evaluated based on the grain interior capacitance, and at 300 °C, it is 331 in the H_2O-humidified atmosphere. This value is approximately 3 times higher than those reported for $BaZr_{0.9}Y_{0.1}O_3$[27] and 6 times higher than that of $BaZr_{0.8}Y_{0.2}O_3$.[26] High dielectric permittivity (above 100) in the $Ba(Zr,Ti,Sn,Hf,Me)O_3$ (where Me = Ta, Nb) high-entropy perovskites was observed by Zhou et al.[44] and in NaCl-type high-entropy oxides by Bérardan et al.[45]

Based on equations (eqs 5−7), the following parameters describing the space-charge barriers were found. In H_2O-wet air at 300 °C, φ_0, the Debye length, and the SCL thickness were 0.18 V, 0.26, and 1.0 nm, respectively. The space-charge barriers at higher temperatures are gathered in Table S5. Moreover, the concentration distribution of proton defects in the vicinity of grain boundary at 300 °C was modeled and is presented in Figure 8. The proton defect concentration in the region adjacent to the grain boundary core is lower by less than two orders of magnitude than that in the bulk. Such a difference is lower than reported for, e.g., $BaZr_{0.9}Y_{0.1}O_{3-x}$ by Kjølseth et al. where the difference at 300 °C is more than three orders of magnitude. Summing up, the characteristics of the grain boundary conduction reported in this work in the multicomponent perovskite differ from that of other materials based on barium zirconate. In particular, the potential barrier, φ_0, is lower than those of low-entropy barium zirconates. For instance, at 300 °C in $BaZr_{0.9}Y_{0.1}O_{3-x}$, Kjølseth et al. determined 0.51−0.62 V in wet oxygen[27] and in $BaZr_{0.8}Y_{0.2}O_{3-x}$ and $BaZr_{0.9}Gd_{0.1}O_{3-x}$, Iguchi et al. found 0.45 and 0.30 V at 200 °C in wet air, respectively.[41] Also, the space-charge layer thickness in $BaZr_{1/8}Hf_{1/8}Sn_{1/8}Ti_{1/8}Y_{1/8}In_{1/8}Sm_{1/8}Yb_{1/8}O_{3-x}$ (1.0 nm) is four times lower than in $BaZr_{0.9}Y_{0.1}O_{3-x}$, which Kjølseth et al. found at 300 °C in wet oxygen as about 4 nm.[27] A relatively low space-charge layer potential may be caused by a high content of acceptor constituents and by short-range disorder present in the grains. The high content of acceptors may lead to the accumulation of negatively charged acceptors in grain boundaries. This partially compensates for the positive charge of the GB core and reduces the depletion of the space-charge layer in positive defects. Such an effect was observed by Iguchi et al. in barium zirconate doped with yttrium and gadolinium.[41] They found the grain boundaries enriched in acceptors by 16, 21, 26, and 24% in $BaZr_{1-x}Y_xO_3$ with x = 0.05, 0.1, 0.15, and 0.20 and $BaZr_{0.9}Gd_{0.1}O_{3-x}$ corresponded to the potential barriers of 0.5, 0.40, 0.43, 0.35, and 0.30 V, respectively. What is more, the short-range disorder present in multicomponent oxides may result in a smaller difference between mobile defect energies in the bulk and the grain boundary cores, leading to a decreased grain boundary potential.

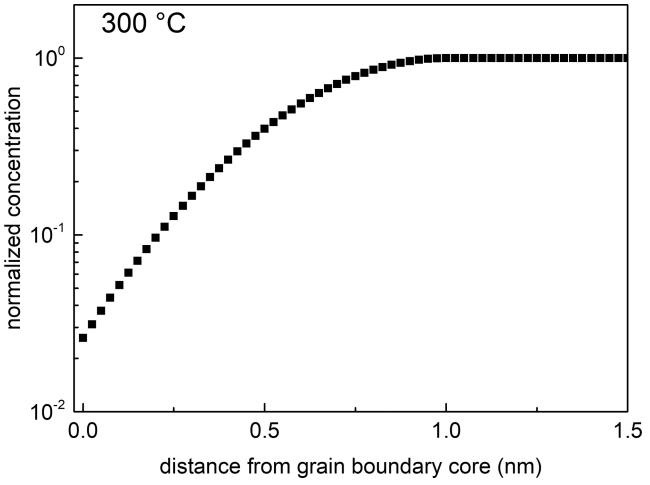

Figure 8. Normalized concentration of proton defects in the space-charge layer relative to the concentration in the grain interior at 300 °C. The plot is a modeled approximation of the space-charge layer.

In view of a relatively low energy barrier related to the space-charge layer at grain boundaries, it seems strange that the activation energy of the specific grain boundary conductivity is nearly 1.2 eV. It suggests that other reasons should also be considered. For example, Yue et al. using quantum mechanical and molecular mechanical simulations found that in the regions of grain boundaries and dislocation cores in $BaZrO_3$, the activation energy of proton transfer is increased because of the contribution of local lattice deformation.[46] In addition, a more prosaic reason, that is, the presence of NiO, which was used as a sintering aid, may partially explain high activation energy. For more information considering the transport properties, please see the Supporting Information file.

3.4. Transport Properties upon Hydration. Further studies of transport properties related to mobile proton defects were carried out by electrical conductivity relaxation (ECR). For the diffusion coefficient estimation, the data were normalized according to eq 8

$$\sigma_n = \frac{\sigma_t - \sigma_0}{\sigma_\infty - \sigma_0} \tag{8}$$

where σ_n is the normalized conductivity, $\sigma_0 = \sigma(t = 0)$ is the initial conductivity, $\sigma_\infty = \sigma(t = \infty)$ is the final conductivity, and $\sigma_t = \sigma(t)$ is the apparent conductivity at time t.[47] In Figure 9, exemplary ECR data recorded at 450 °C are shown. As can be noticed, the relaxation curve is single-fold, indicating a coupled transport of hydrogen and oxygen ions in the structure.[48] A two-step (nonmonotonic) process, which occurs only if sufficiently high hole conductivity is present,[49] was not observed in the studied temperature range (below 600 °C). The condition for the evaluation of $D_{OH^\bullet}$ and $k_{OH^\bullet}$ at the same time depends on the relation between them and the sample thickness.[50,51] Accurate determination of both coefficients is possible when the relation (eq 9) is fulfilled

$$0.03 \le L = \frac{l \cdot k}{D} \le 30 \tag{9}$$

where L is a dimensionless parameter, l is half of the thickness of the sample, k is the chemical surface exchange coefficient, and D is the chemical diffusion coefficient. When $L \gg 30$, the process is diffusion-dominated, whereas if $L \ll 0.03$,

https://doi.org/10.1021/acs.jpcc.3c03906
J. Phys. Chem. C 2023, 127, 14534−14544

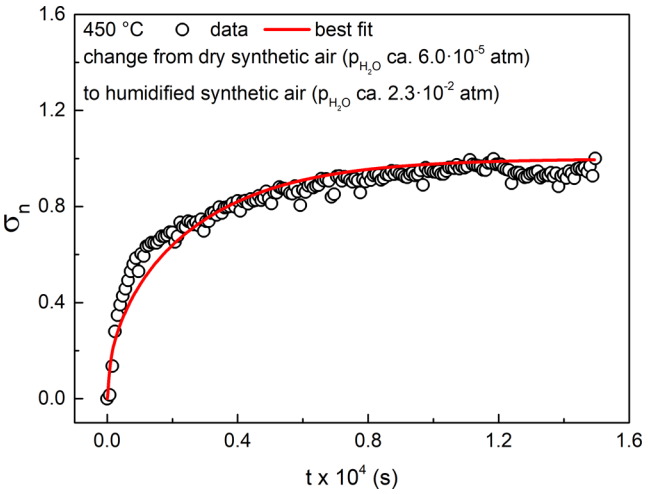

Figure 9. Total electrical conductivity relaxation (ECR) data at 450 °C during the change of the atmosphere from dry to humidified. The red line represents the fitted curve. The estimated error is 4.5%; thus, the error bars are not included as they would be smaller than the data points in the plots.

the process is controlled by the surface reaction. The values of transport coefficients and the dimensionless parameter L are summarized in Table 2. The condition for the simultaneous determination of $D_{OH^\bullet}$ and $k_{OH^\bullet}$ is fulfilled for all temperatures apart from 450 °C. The derived $D_{OH^\bullet}$ values and the surface exchange coefficients $k_{OH^\bullet}$ are in the 10^{-8}–10^{-6} cm^2 s^{-1} and the 10^{-6}–10^{-4} cm s^{-1} range, respectively. All data along with the respective energies are presented in Figure 10.

Table 2. Diffusion Coefficients ($D_{OH^\bullet}$), Surface Exchange Coefficients ($k_{OH^\bullet}$), and Dimensionless L Parameters Calculated Based on Conductivity Relaxation Measurements for $BaZr_{1/8}Hf_{1/8}Sn_{1/8}Ti_{1/8}Y_{1/8}In_{1/8}Sm_{1/8}Yb_{1/8}O_{3-x}$

T (°C)	$D_{OH^\bullet}$ (cm^2 s^{-1})	$k_{OH^\bullet}$ (cm s^{-1})	L
600	1.9(1) × 10^{-6}	9.6(1) × 10^{-4}	20.0
500	3.0(1) × 10^{-7}	1.6(1) × 10^{-4}	21.7
400	1.2(1) × 10^{-7}	8.4(1) × 10^{-5}	27.5
300	2.2(1) × 10^{-8}	5.7(1) × 10^{-6}	10.2

The activation energy associated with the water chemical diffusion was estimated as 0.66 eV, which is very close to the activation energy of bulk conductivity (0.67 eV) and lower than the one of total conductivity (0.90 eV) in wet air at temperatures below 500 °C. Conductivity and chemical diffusion are related but not identical transport processes of proton defects and oxygen vacancies. Conductivity is the quasi-independent transport of both types of charge forced by a weak electric field, whereas, in the case of chemical diffusion, the transport is coupled and occurs under a large concentration gradient since the space-charge potential and thickness of grain boundaries are not linear properties, which means they are influenced by a large concentration gradient. Therefore, the differences between the activation energies of total conductivity and chemical diffusion should be expected. The values of transport coefficients are comparable to the previously reported barium–zirconium system. For example, for $Ba_{0.9}La_{0.1}Zr_{0.25}Sn_{0.25}In_{0.5}O_{3-a}$, the coefficient $D_{OH^\bullet}$ is in a range from 10^{-8} to 10^{-5} cm^2 s^{-1} at a 300–600 °C temperature

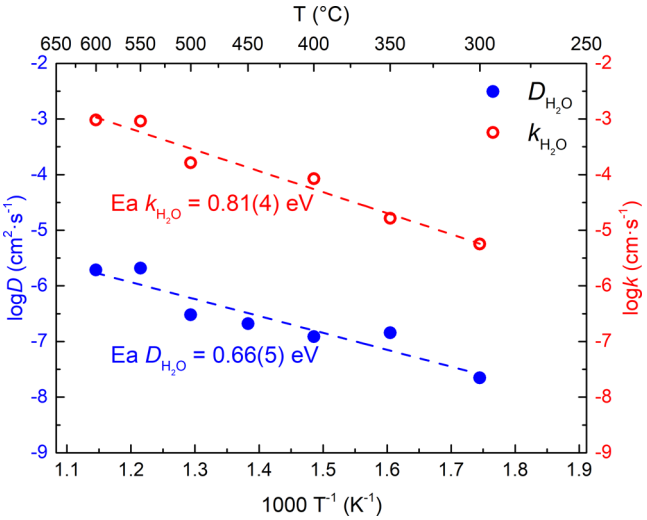

Figure 10. Temperature dependence of the D (blue) and k (red) with calculated values of the activation energy. Data are shown in Arrhenius-type coordinates. As the estimated error for most points is less than 5%, the error bars are not included as they would be smaller than the point on the figure. For the standard deviation of fittings of electrical conductivity relaxation curves in a 300–600 °C temperature range, please see Table S7.

range and the chemical surface exchange coefficient $k_{OH^\bullet}$ is from 10^{-6} to 10^{-2} cm s^{-1}[52] in the same range. Additionally, these values are higher than those published for some other proton-conducting perovskites such as indium-doped $SrCeO_3$ for which $D_{OH^\bullet}$ is in the range of 10^{-6}–10^{-7} cm^2 s^{-1} and $k_{OH^\bullet}$ is 10^{-5}–10^{-6} cm s^{-1}[53] at 500–700 °C. For more information considering the diffusion properties, please see the Supporting Information File.

4. CONCLUSIONS

Transport properties of single-phase $BaZr_{1/8}Hf_{1/8}Sn_{1/8}Ti_{1/8}Y_{1/8}In_{1/8}Sm_{1/8}Yb_{1/8}O_{3-x}$ as an exemplary member of multicomponent perovskites with mixed conductivity were presented and discussed.

The presence of proton defects was shown using thermogravimetry, while the conductivity isotope effect and the ECR results confirmed proton conduction occurring by the Grotthuss mechanism. The presence of proton defects caused the expansion of the unit cell and influenced the thermal expansion coefficient. The significant content of proton defects was observed below 500 °C, whereas the dehydration process kinetics was found to be slow.

The single-fold relaxation curves below 600 °C indicated that the electronic conductivity in the $BaZr_{1/8}Hf_{1/8}Sn_{1/8}Ti_{1/8}Y_{1/8}In_{1/8}Sm_{1/8}Yb_{1/8}O_{3-x}$ high-entropy oxide may be neglected. With the proton transport numbers for total conductivity in the range of 0.04–0.59 in H_2O-humidified air, we may conclude that the transport properties are dominated by two mobile ionic defects: proton defects, $OH_O^\bullet$, and oxygen vacancies, $V_O^{\bullet\bullet}$.

A large content of acceptor constituents was proposed as a possible reason for a relatively high activation energy of bulk conductivity below 500 °C in wet air (0.67 eV) and a low space-charge layer potential barrier (0.18 V at 300 °C in H_2O-humidified air) and thickness (3.5 nm) at grain boundaries. The potential barrier height is significantly lower than those observed for typical polycrystalline-doped barium zirconates.

https://doi.org/10.1021/acs.jpcc.3c03906
J. Phys. Chem. C 2023, 127, 14534–14544

For the first time in the case of high-entropy materials, the chemical diffusion coefficient $D_{OH^\bullet}$ and chemical surface exchange coefficient $k_{OH^\bullet}$ of water were determined based on electrical conductivity relaxation (ECR) experiments. The chemical diffusion coefficient of water $D_{OH^\bullet}$ and the surface exchange coefficient $k_{OH^\bullet}$ are is in the range of $2.2(1) \times 10^{-8}$–$1.9(1) \times 10^{-6}$ cm^2 s^{-1} and $5.7(1) \times 10^{-6}$–$9.6(1) \times 10^{-4}$ cm s^{-1}, respectively.

■ ASSOCIATED CONTENT

Supporting Information

The Supporting Information is available free of charge at https://pubs.acs.org/doi/10.1021/acs.jpcc.3c03906.

Structural—HT-XRD structural data; microstructural—SEM and EDS results; impedance data—exemplary Nyquist impedance spectra; bulk and grain boundary determination procedures; and values of the potential at a grain boundary (PDF)

■ AUTHOR INFORMATION

Corresponding Author

Wojciech Skubida − *Institute of Nanotechnology and Materials Engineering, and Advanced Materials Centre, Gdańsk University of Technology, 80-233 Gdańsk, Poland;* orcid.org/0000-0003-3036-4975; Email: wojciech.skubida@pg.edu.pl

Authors

Daniel Jaworski − *Institute of Nanotechnology and Materials Engineering, and Advanced Materials Centre, Gdańsk University of Technology, 80-233 Gdańsk, Poland;* orcid.org/0000-0001-5791-6413

Aleksandra Mielewczyk-Gryń − *Institute of Nanotechnology and Materials Engineering, and Advanced Materials Centre, Gdańsk University of Technology, 80-233 Gdańsk, Poland*

Sebastian Wachowski − *Institute of Nanotechnology and Materials Engineering, and Advanced Materials Centre, Gdańsk University of Technology, 80-233 Gdańsk, Poland;* orcid.org/0000-0003-3752-0432

Tadeusz Miruszewski − *Institute of Nanotechnology and Materials Engineering, and Advanced Materials Centre, Gdańsk University of Technology, 80-233 Gdańsk, Poland*

Kacper Cichy − *Faculty of Energy and Fuels, Department of Hydrogen Energy, AGH University of Science and Technology, 30-059 Kraków, Poland;* orcid.org/0000-0002-5770-6974

Konrad Świerczek − *Faculty of Energy and Fuels, Department of Hydrogen Energy, AGH University of Science and Technology, 30-059 Kraków, Poland; AGH Centre of Energy, AGH University of Science and Technology, 30-054 Kraków, Poland;* orcid.org/0000-0003-4519-389X

Maria Gazda − *Institute of Nanotechnology and Materials Engineering, and Advanced Materials Centre, Gdańsk University of Technology, 80-233 Gdańsk, Poland;* orcid.org/0000-0001-6193-7815

Complete contact information is available at: https://pubs.acs.org/10.1021/acs.jpcc.3c03906

Notes

The authors declare no competing financial interest.

■ ACKNOWLEDGMENTS

This project was funded by the National Science Centre, Poland, on the basis of the decision number 2019/35/B/ST5/00888.

■ REFERENCES

(1) Yoo, H.-I.; Schmalzried, H.; Martin, M.; Janek, J. Cross Effect Between Electronic and Ionic Flows in Semiconducting Transition Metal Oxides. *Z. Phys. Chem.* **1990**, *168*, 129−142.

(2) Fuel Cells and Hydrogen Energy. In *Perovskite Oxide for Solid Oxide Fuel Cells*; Ishihara, T., Ed.; Springer: Boston, MA, US, 2009.

(3) Jiang, S.; Hu, T.; Gild, J.; Zhou, N.; Nie, J.; Qin, M.; Harrington, T.; Vecchio, K.; Luo, J. A New Class of High-Entropy Perovskite Oxides. *Scr. Mater.* **2018**, *142*, 116−120.

(4) Shi, Y.; Ni, N.; Ding, Q.; Zhao, X. Tailoring High-Temperature Stability and Electrical Conductivity of High Entropy Lanthanum Manganite for Solid Oxide Fuel Cell Cathodes. *J. Mater. Chem. A* **2022**, *10*, 2256−2270.

(5) Gild, J.; Samiee, M.; Braun, J. L.; Harrington, T.; Vega, H.; Hopkins, P. E.; Vecchio, K.; Luo, J. High-Entropy Fluorite Oxides. *J. Eur. Ceram. Soc.* **2018**, *38*, 3578−3584.

(6) Bonnet, E.; Grenier, J. C.; Bassat, J. M.; Jacob, A.; Delatouche, B.; Bourdais, S. On the Ionic Conductivity of Some Zirconia-Derived High-Entropy Oxides. *J. Eur. Ceram. Soc.* **2021**, *41*, 4505−4515.

(7) Bérardan, D.; Franger, S.; Meena, A. K.; Dragoe, N. Room Temperature Lithium Superionic Conductivity in High Entropy Oxides. *J. Mater. Chem. A* **2016**, *4*, 9536−9541.

(8) Zeng, Y.; Ouyang, B.; Liu, J.; Byeon, Y.-W.; Cai, Z.; Miara, L. J.; Wang, Y.; Ceder, G. High-Entropy Mechanism to Boost Ionic Conductivity. *Science* **2022**, *378*, 1320−1324.

(9) Gazda, M.; Miruszewski, T.; Jaworski, D.; Mielewczyk-Gryń, A.; Skubida, W.; Wachowski, S.; Winiarz, P.; Dzierzgowski, K.; Łapiński, M.; Szpunar, I.; Dzik, E. Novel Class of Proton Conducting Materials-High Entropy Oxides. *ACS Mater. Lett.* **2020**, *2*, 1315−1321.

(10) Dippo, O. F.; Vecchio, K. S. A Universal Configurational Entropy Metric for High-Entropy Materials. *Scr. Mater.* **2021**, *201*, No. 113974.

(11) *Advanced Nano Deposition Methods*; Lin, Y.; Chen, X., Eds.; Wiley-VCH Verlag GmbH & Co. KGaA: Weinheim, Germany, 2016.

(12) Ciucci, F. Electrical Conductivity Relaxation Measurements: Statistical Investigations Using Sensitivity Analysis, Optimal Experimental Design and ECRTOOLS. *Solid State Ionics* **2013**, *239*, 28−40.

(13) Welch, M. D. R. H. Mitchell Perovskites Modern and Ancient. Thunder Bay, Ontario (Almaz Press, Www.Almaz-Press.Com) 2002. 316 Pp. Price US $70.00 (+ Shipping and Handling). ISBN 0 9689411 0 9. *Mineral. Mag.* **2003**, *67*, 419−420.

(14) Andersson, A. K. E.; Selbach, S. M.; Knee, C. S.; Grande, T. Chemical Expansion Due to Hydration of Proton-Conducting Perovskite Oxide Ceramics. *J. Am. Ceram. Soc.* **2014**, *97*, 2654−2661.

(15) Colomban, P.; Tran, C.; Zaafrani, O.; Slodczyk, A. Aqua Oxyhydroxycarbonate Second Phases at the Surface of Ba/Sr-Based Proton Conducting Perovskites: A Source of Confusion in the Understanding of Proton Conduction: Second Phases at the Surface of Ba/Sr-Based Proton Conductors. *J. Raman Spectrosc.* **2013**, *44*, 312−320.

(16) Colomban, P.; Zaafrani, O.; Slodczyk, A. Proton Content and Nature in Perovskite Ceramic Membranes for Medium Temperature Fuel Cells and Electrolysers. *Membranes* **2012**, *2*, 493−509.

(17) Gonçalves, M. D.; Mielewczyk-Gryń, A.; Maram, P. S.; Kryścio, Ł.; Gazda, M.; Navrotsky, A. Systematic Water Uptake Energetics of Yttrium-Doped Barium Zirconate-A High Resolution Thermochemical Study. *J. Phys. Chem. C* **2020**, *124*, 11308−11316.

(18) Norby, T.; Widerøe, M.; Glöckner, R.; Larring, Y. Hydrogen in Oxides. *Dalton Trans.* **2004**, 3012−3018.

(19) Little, E. J.; Jones, M. M. A Complete Table of Electronegativities. *J. Chem. Educ.* **1960**, *37*, No. 231.

(20) Mielewczyk-Gryń, A.; Subramani, T.; Jaworski, D.; Lilova, K.; Skubida, W.; Navrotsky, A.; Gazda, M. Water Uptake and Energetics

of the Formation of Barium Zirconate Based Multicomponent Oxides. *Phys. Chem. Chem. Phys.* **2023**, *25*, 9208−9215.
(21) Torino, N.; Henry, P. F.; Knee, C. S.; Callear, S. K.; Smith, R. I.; Rahman, S. M. H.; Eriksson, S. G. Insight into the Dehydration Behaviour of Scandium-Substituted Barium Titanate Perovskites via Simultaneous in Situ Neutron Powder Thermodiffractometry and Thermogravimetric Analysis. *Solid State Ionics* **2018**, *324*, 233−240.
(22) Han, D.; Hatada, N.; Uda, T. Chemical Expansion of Yttrium-Doped Barium Zirconate and Correlation with Proton Concentration and Conductivity. *J. Am. Ceram. Soc.* **2016**, *99*, 3745−3753.
(23) Cichy, K.; Skubida, W.; Świerczek, K. Structural Transformations, Water Incorporation and Transport Properties of Tin-Substituted Barium Indate. *J. Solid State Chem.* **2018**, *262*, 58−67.
(24) Løken, A.; Ricote, S.; Wachowski, S. Thermal and Chemical Expansion in Proton Ceramic Electrolytes and Compatible Electrodes. *Crystals* **2018**, *8*, No. 365.
(25) Lim, D.-K.; Park, C.-J.; Choi, M.-B.; Park, C.-N.; Song, S.-J. Partial Conductivities of Mixed Conducting BaCe0.65Zr0.2Y0.15O3−*δ*. *Int. J. Hydrogen Energy* **2010**, *35*, 10624−10629.
(26) Babilo, P.; Uda, T.; Haile, S. M. Processing of Yttrium-Doped Barium Zirconate for High Proton Conductivity. *J. Mater. Res.* **2007**, *22*, 1322−1330.
(27) Kjølseth, C.; Fjeld, H.; Prytz, Ø.; Dahl, P. I.; Estournès, C.; Haugsrud, R.; Norby, T. Space−Charge Theory Applied to the Grain Boundary Impedance of Proton Conducting BaZr0.9Y0.1O3−*δ*. *Solid State Ionics* **2010**, *181*, 268−275.
(28) Bonanos, N.; Huijser, A.; Poulsen, F. W. H/D Isotope Effects in High Temperature Proton Conductors. *Solid State Ionics* **2015**, *275*, 9−13.
(29) Bonanos, N. Oxide-Based Protonic Conductors: Point Defects and Transport Properties. *Solid State Ionics* **2001**, *145*, 265−274.
(30) Zhang, G. Protonic Conduction in Ba2In2O5. *Solid State Ionics* **1995**, *82*, 153−160.
(31) Han, D.; Noda, Y.; Onishi, T.; Hatada, N.; Majima, M.; Uda, T. Transport Properties of Acceptor-Doped Barium Zirconate by Electromotive Force Measurements. *Int. J. Hydrogen Energy* **2016**, *41*, 14897−14908.
(32) Satapathy, A.; Sinha, E.; Rout, S. K. Investigation of Proton Conductivity in Sc and Yb Co-Doped Barium Zirconate Ceramics. *Mater. Res. Express* **2019**, *6*, No. 056305.
(33) Yang, W.; Wang, L.; Li, Y.; Zhou, H.; He, Z.; Han, C.; Dai, L. An Easily Sintered, Chemically Stable Indium and Tin Co-Doped Barium Hafnate Electrolyte for Hydrogen Separation. *J. Alloys Compd.* **2021**, *868*, No. 159117.
(34) Gilardi, E.; Fabbri, E.; Bi, L.; Rupp, J. L. M.; Lippert, T.; Pergolesi, D.; Traversa, E. Effect of Dopant−Host Ionic Radii Mismatch on Acceptor-Doped Barium Zirconate Microstructure and Proton Conductivity. *J. Phys. Chem. C* **2017**, *121*, 9739−9747.
(35) Zhu, Z.; Wang, S. Investigation on Samarium and Yttrium Co-Doping Barium Zirconate Proton Conductors for Protonic Ceramic Fuel Cells. *Ceram. Int.* **2019**, *45*, 19289−19296.
(36) Bohn, H. G.; Schober, T. Electrical Conductivity of the High-Temperature Proton Conductor BaZr0.9Y0.1O2.95. *J. Am. Ceram. Soc.* **2004**, *83*, 768−772.
(37) Draber, F. M.; Ader, C.; Arnold, J. P.; Eisele, S.; Grieshammer, S.; Yamaguchi, S.; Martin, M. Nanoscale Percolation in Doped BaZrO3 for High Proton Mobility. *Nat. Mater.* **2020**, *19*, 338−346.
(38) Draber, F. M.; Draber, F. M. *Ionic Conductivity in Acceptor-Doped Barium Zirconate*, Doctoral Dissertation, Dissertation; RWTH Aachen University, 2021.
(39) Yamazaki, Y.; Blanc, F.; Okuyama, Y.; Buannic, L.; Lucio-Vega, J. C.; Grey, C. P.; Haile, S. M. Proton Trapping in Yttrium-Doped Barium Zirconate. *Nat. Mater.* **2013**, *12*, 647−651.
(40) Bjorketun, M.; Sundell, P.; Wahnstrom, G.; Engberg, D. A Kinetic Monte Carlo Study of Proton Diffusion in Disordered Perovskite Structured Lattices Based on First-Principles Calculations. *Solid State Ionics* **2005**, *176*, 3035−3040.
(41) Iguchi, F.; Sata, N.; Yugami, H. Proton Transport Properties at the Grain Boundary of Barium Zirconate Based Proton Conductors for Intermediate Temperature Operating SOFC. *J. Mater. Chem.* **2010**, *20*, No. 6265.
(42) Guo, X.; Maier, J. Grain Boundary Blocking Effect in Zirconia: A Schottky Barrier Analysis. *J. Electrochem. Soc.* **2001**, *148*, No. E121.
(43) Fleig, J. The Grain Boundary Impedance of Random Microstructures: Numerical Simulations and Implications for the Analysis of Experimental Data. *Solid State Ionics* **2002**, *150*, 181−193.
(44) Zhou, S.; Pu, Y.; Zhang, Q.; Shi, R.; Guo, X.; Wang, W.; Ji, J.; Wei, T.; Ouyang, T. Microstructure and Dielectric Properties of High Entropy Ba(Zr0.2Ti0.2Sn0.2Hf0.2Me0.2)O3 Perovskite Oxides. *Ceram. Int.* **2020**, *46*, 7430−7437.
(45) Bérardan, D.; Franger, S.; Dragoe, D.; Meena, A. K.; Dragoe, N. Colossal Dielectric Constant in High Entropy Oxides. *Phys. Status Solidi RRL* **2016**, *10*, 328−333.
(46) Yue, S.; Zhao, J.; Sun, Y.; Niu, H.; Li, H.; Jing, Y.; Aluru, N. R. Multi-Scale Simulation of Proton Diffusion in Dislocation Cores in $BaZrO_3$. *Phys. Chem. Chem. Phys.* **2022**, *24*, 21440−21451.
(47) Na, B. T.; Yang, T.; Liu, J.; Lee, S.; Abernathy, H.; Kalapos, T.; Hackett, G. Enhanced Accuracy of Electrochemical Kinetic Parameters Determined by Electrical Conductivity Relaxation. *Solid State Ionics* **2021**, *361*, No. 115561.
(48) Yoo, H.-I.; Yeon, J. I.; Kim, J.-K. Mass Relaxation vs. Electrical Conductivity Relaxation of a Proton Conducting Oxide upon Hydration and Dehydration. *Solid State Ionics* **2009**, *180*, 1443−1447.
(49) Lim, D.-K.; Choi, M.-B.; Lee, K.-T.; Yoon, H.-S.; Wachsman, E. D.; Song, S.-J. Conductivity Relaxation of Proton-Conducting BaCe0.85Y0.15O3−*δ* Upon Oxidation and Reduction. *J. Electrochem. Soc.* **2011**, *158*, No. B852.
(50) Williams, M. M. R. The Mathematics of Diffusion. *Ann. Nucl. Energy* **1977**, *4*, 205−206.
(51) Lee, D.; Yoo, H. Unusual Oxygen Re-Equilibration Kinetics of TiO2−*δ*. *Solid State Ionics* **2006**, *177*, 1−9.
(52) Skubida, W.; Niemczyk, A.; Zheng, K.; Liu, X.; Świeczek, K. Crystal Structure, Hydration, and Two-Fold/Single-Fold Diffusion Kinetics in Proton-Conducting Ba0.9La0.1Zr0.25Sn0.25In0.5O3−a Oxide. *Crystals* **2018**, *8*, No. 136.
(53) Skubida, W.; Zheng, K.; Świerczek, K.; Michna, M.; Kondracki, Ł. Indium Doping in SrCeO3 Proton-Conducting Perovskites. *J. Solid State Chem.* **2020**, *284*, No. 121210.

https://doi.org/10.1021/acs.jpcc.3c03906
J. Phys. Chem. C 2023, 127, 14534−14544